Research Square

Preprints are preliminary reports that have not undergone peer review.
They should not be considered conclusive, used to inform clinical practice,
or referenced by the media as validated information.

A Comb-Shaped, Silicone-Scaffolded Hydrogel Electrode for Stable Overnight EEG Acquisition in Assistive BCI Applications

Weihua Pei

peiwh@semi.ac.cn

Institute of Semiconductors, Chinese Academy of Sciences https://orcid.org/0000-0002-1631-0199

Wanwan Liu

School of Physics and Optoelectronics, Xiangtan University

Chunrong Wei

School of Physics and Optoelectronics, Xiangtan University https://orcid.org/0000-0002-0834-9077

Hongyu Jiang

School of Physics and Optoelectronics, Xiangtan University

Yan Zhu

School of Physics and Optoelectronics, Xiangtan University

Kemin Wang

Hunan Institute of Advanced Sensing and Information Technology, Xiangtan University

Xiaoting Wu

School of Computer Science and Artificial Intelligence, Shanxi Normal University

Juexian Cao

Hunan Institute of Advanced Sensing and Information Technology, Xiangtan University

Xiaofeng Liu

Xiangtan University https://orcid.org/0000-0002-0447-5658

Yiwei Liu

Hunan Institute of Advanced Sensing and Information Technology, Xiangtan University

Gege Ming

nstitute of Semiconductors, Chinese Academy of Sciences

Yijun Wang

Institute of Semiconductors, Chinese Academy of Sciences

Xiaorong Gao

Department of Biomedical Engineering, School of Medicine, Tsinghua University

Article

Keywords:

Posted Date: April 23rd, 2026

DOI: https://doi.org/10.21203/rs.3.rs-9381602/v1

License: This work is licensed under a Creative Commons Attribution 4.0 International License.
Read Full License

Additional Declarations: There is no conflict of interest

A Comb-Shaped, Silicone-Scaffolded Hydrogel Electrode for Stable Overnight EEG Acquisition in Assistive BCI Applications

Wanwan Liu[1], Chunrong Wei[1]*, Hongyu Jiang[1], Yan Zhu[1], Kemin Wang[2], Weihua Pei[3]*, Xiaoting Wu[4], Juexian Cao[2], Xiaofeng Liu[2], Yiwei Liu[2], Gege Ming[5], Yijun Wang[3] and Xiaorong Gao[5]

[1] School of Physics and Optoelectronics, Xiangtan University, Xiangtan 411105, China.

[2] Hunan Institute of Advanced Sensing and Information Technology, Xiangtan University, Xiangtan 411105, China.

[3] State Key Laboratory of Integrated Optoelectronics, Institute of Semiconductors, Chinese Academy of Sciences, Beijing 100083, China.

[4] School of Computer Science and Artificial Intelligence, Shanxi Normal University, Taiyuan 030031, China.

[5] Department of Biomedical Engineering, School of Medicine, Tsinghua University, Beijing 100084, China.

Wanwan Liu: 202305820101@smail.xtu.edu.cn

Chunrong Wei*: weichunrong1224@163.com (Corresponding author)

Hongyu Jiang: 2575307930@qq.com

Yan Zhu: zhuyan13324@163.com

Kemin Wang: 1205809434@qq.com

Weihua Pei*: peiwh@semi.ac.cn (Corresponding author)

Xiaoting Wu: 15735176537@163.com

Juexian Cao: jxcao@xtu.edu.cn

Xiaofeng Liu: lxf0301@xtu.edu.cn

Yiwei Liu: yiweiliu@xtu.edu.cn

Gege Ming: minggege@semi.ac.cn

Yijun Wang: wangyj@semi.ac.cn

Xiaorong Gao: gxr-dea@tsinghua.edu.cn

Abstract

For older adults with disabilities and aphasia, timely care remains challenging, particularly during the 8-h nocturnal period, creating a need for stable non-invasive EEG interfaces for assistive brain-computer interface (BCI) applications. Asynchronous steady-state visual evoked potential (SSVEP)-based control provides a practical strategy for nighttime assistive care, but its performance is largely constrained by the electrode interface. Here, we developed a comb-shaped, silicone-scaffolded PVA/SA/PEDOT:PSS hydrogel electrode for stable overnight EEG acquisition on hair-bearing scalp regions. The PVA/SA network provided soft and compliant contact, while PEDOT:PSS improved interfacial charge transfer. The comb-shaped silicone scaffold further enhanced conformal contact and effectively suppressed hydrogel dehydration. The electrode maintained stable scalp impedance for 8 h and enabled reliable EEG recording on both hairless and hair-bearing scalp regions. When used in an asynchronous SSVEP-based intelligent assistive care system, it achieved 100% triple-blink (three consecutive blinks) detection accuracy for system activation and 97.3 ± 0.4% SSVEP classification accuracy for command selection, with stable performance throughout the 8-h monitoring period. Cytotoxicity assays indicated no obvious cytotoxicity under the tested conditions, and comfort evaluations supported good wearability. This hydrogel electrode provides a promising approach for non-invasive and reliable overnight EEG acquisition and shows potential for BCI-assisted nighttime care.

Introduction

With global population aging and persistently high stroke incidence, the rising prevalence of disabilities and aphasia is placing mounting pressure on long-term care[1–3]. These pressures are particularly acute during the nocturnal period, when sustained caregiving over an 8-h window places substantial physical demands on caregivers. Such demands can make timely responses to patients' needs more difficult, thereby increasing psychological stress on patients[4–6]. Brain-computer interface (BCI) technology, particularly non-invasive steady-state visual evoked potential (SSVEP)-based paradigms, represents a promising strategy for nighttime assistive care[7–10]. SSVEP-BCI systems can acquire and decode electroencephalography (EEG) signals to generate control commands for assistive devices, thereby enabling self-care tasks and reducing reliance on continuous overnight supervision[11–13]. The primary challenge is to achieve high-quality EEG acquisition with both overnight stability and wear comfort.

A stable, low-impedance skin-electrode interface is essential for high-quality EEG acquisition during 8-h overnight monitoring[13–16]. Traditional wet electrodes utilize electrolyte gels to establish stable ionic conduction pathways, enabling low interfacial impedance and high signal-to-noise ratio (SNR)[17, 18]. However, the fluid nature of wet electrodes poses a risk of short circuits between adjacent electrodes, while prolonged skin contact increases the risk

of skin irritation[19, 20]. Furthermore, the rapid dehydration of the electrolyte induces interfacial instability and progressive signal degradation, limiting their reliability and suitability for continuous nocturnal EEG monitoring[20, 21]. Composed of conductive materials such as metals, fabrics, and polymers, dry electrodes exhibit high, pressure-dependent impedance, leading to excessive noise and signal distortion[22–24]. While increased headband pressure can modestly reduce interfacial impedance, it significantly compromises wearer comfort, which undermines long-term wearability and high-fidelity EEG acquisition[24, 25]. Semi-dry electrodes represent an intermediate strategy between wet and dry electrodes, with electrolyte stored in a porous or capillary matrix to sustain hydration at the skin-electrode interface[26, 27]. However, semi-dry electrodes still face practical challenges for prolonged monitoring, including limited electrolyte supply, gradual interfacial deterioration, and difficulty in maintaining stable and comfortable skin contact.

Hydrogel-based electrodes offer an attractive alternative by immobilizing the electrolyte within a crosslinked polymer network, enabling uniform and sustained ionic conduction with minimal leakage[28, 29]. Their low modulus and inherent softness facilitate conformal skin contact and suppress interfacial micro-slip, improving signal stability and wear comfort[29–31]. However, hydrogels are prone to persistent dehydration due to continuous water evaporation and migration under dynamic use conditions, leading to material stiffening and progressive signal degradation over time[32, 33]. Various strategies have been explored to mitigate dehydration. Incorporating hygroscopic salts can effectively prevent dehydration and hardening while maintaining high conductivity[32–34]. However, high salt concentrations may cause skin irritation, osmotic stress, and corrosion of integrated metal circuits, compromising device reliability[28]. Alternatively, water-organic solvent binary systems reduce free water content and increase evaporation enthalpy, effectively suppressing dehydration[34, 35]. Nevertheless, organic solvents tend to increase interfacial impedance by raising viscosity and lowering ion mobility[32]. Surface modification strategies, such as applying ultrathin biomimetic or gradient hydrophobic coatings, can suppress water escape by acting as a physical barrier[36, 37]. Yet, such coatings may suffer from reliability issues under practical conditions involving curved scalp geometry and dynamic deformation, potentially leading to mechanical failure such as cracking or delamination[37, 38]. Encapsulation provides another effective strategy for enhancing hydration stability by physically blocking water vapor migration[39, 40]. However, hydrogel-based encapsulation may hinder conformal contact on hair-bearing scalp due to microscopic curvature and hair topography, limiting its suitability for reliable nocturnal EEG monitoring[41–43]. Constructing double-network hydrogels with dense hydrogen-bond crosslinks can improve hydration retention[35]. Nevertheless, higher effective crosslink density often densifies the network, compromising conductivity through restricted ion mobility and hindering wearable conformity due to increased stiffness and reduced extensibility[32]. Consequently, designing hydrogel electrodes that simultaneously

provide sustained hydration, stable electrochemical interfacing, scalp conformability, and unobtrusive comfort remains a significant challenge for continuous nocturnal EEG monitoring.

In this work, we developed a comb-shaped, silicone-scaffolded PVA/SA/PEDOT:PSS hydrogel electrode for stable overnight EEG acquisition on the hair-bearing scalp (Fig. 1). The PVA/SA network was designed to provide soft mechanical compliance and support interfacial hydration. PEDOT:PSS was incorporated as a conductive phase to promote efficient interfacial charge transfer while largely preserving the hydrogen-bonded matrix. The

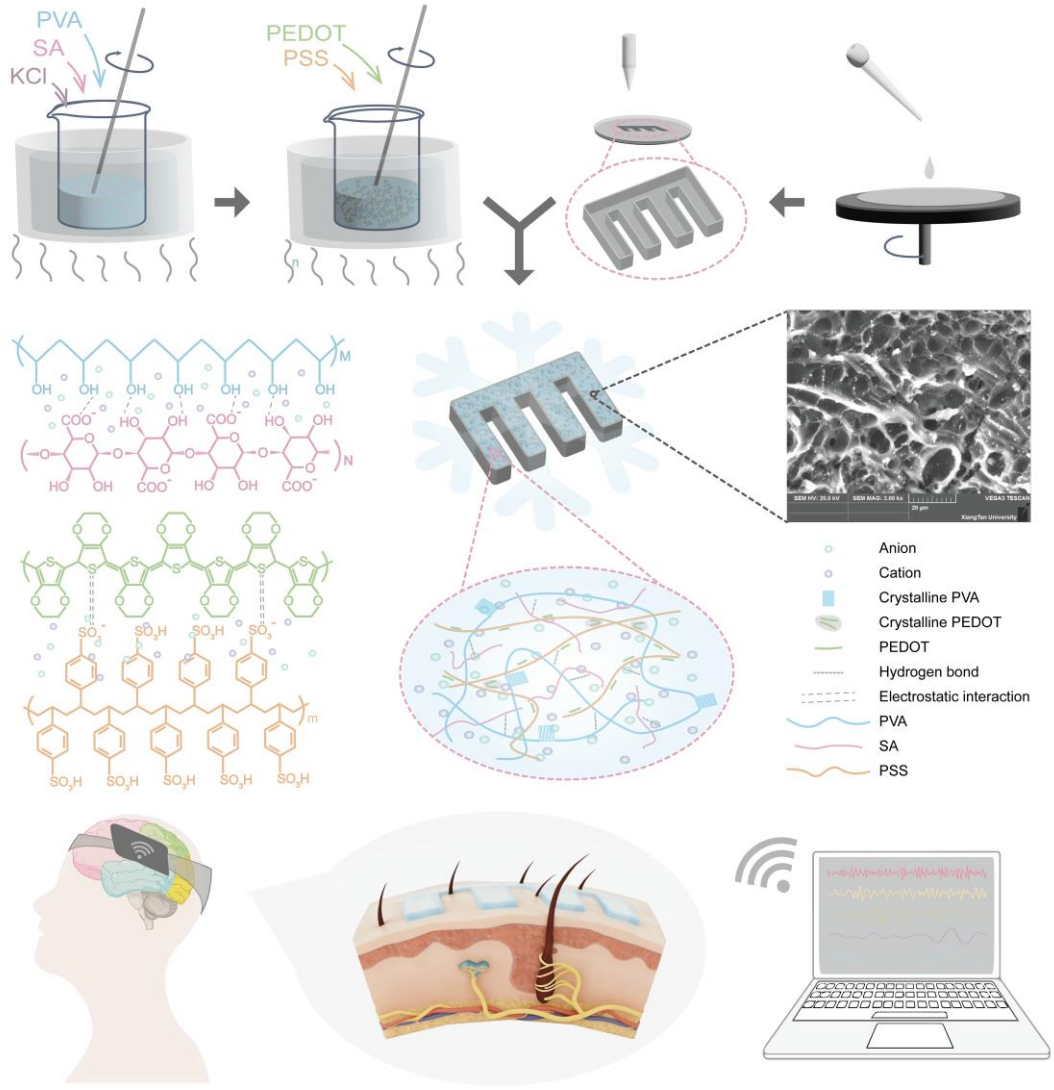


Fig. 1 Schematic illustration of the hydrogel electrode for EEG acquisition.

The figure illustrates the fabrication process of the comb-shaped silicone scaffold and the PVA/SA/PEDOT:PSS hydrogel, along with the physical crosslinking network of the hydrogel and a scanning electron microscopy (SEM) image of the actual network structure. The electrode is fixed on the scalp with gauze for EEG signal acquisition, and the recorded signals are transmitted via Wi-Fi for SSVEP-based BCI control.

comb-shaped silicone scaffold improved conformal contact with the hair-bearing scalp and helped maintain stable hydration during overnight wear. Consequently, the electrode maintained stable scalp impedance for 8 h and enabled reliable EEG recording in both hairless and hair-bearing scalp regions. When used in an asynchronous SSVEP-based intelligent assistive care system, it achieved 100% triple-blink detection accuracy and 97.3 ± 0.4% SSVEP classification accuracy, demonstrating its potential for nighttime assistive BCI applications.

Results

1. Preparation and characterization of the hydrogel electrode

To achieve stable EEG recording on the hair-bearing scalp for 8-h overnight monitoring, we fabricated a comb-shaped, silicone-scaffolded PVA/SA/PEDOT:PSS hydrogel electrode. The PVA/SA network was formed through freeze-thaw-induced physical association, primarily mediated by hydrogen bonding. Fourier-transform infrared (FTIR) spectroscopy yielded evidence consistent with physical crosslinking between PVA and SA (Fig. 2a). Gaussian fitting of the characteristic absorption bands revealed systematic peak shifts and pronounced band broadening in the PVA/SA hydrogel. In the hydroxyl stretching region (3000-3600 cm^{-1}), Gaussian fitting showed that the -OH band center blue-shifted from 3295.87 ± 0.55 cm^{-1} for PVA to 3330.51 ± 10.07 cm^{-1} for PVA/SA, while the full width at half maximum (FWHM) increased from 317.97 ± 2.36 cm^{-1} to 361.97 ± 6.53 cm^{-1} (Fig. 2b). The blue shift and band broadening were consistent with SA-induced changes in the hydrogen-bonding microenvironment of PVA hydroxyl groups, suggesting a broader distribution of hydrogen-bond strengths and increased network heterogeneity. Correspondingly, in the asymmetric carboxylate stretching region (1550-1650 cm^{-1}), the $-COO^-$ band center shifted from 1595.23 ± 0.24 cm^{-1} for SA to 1638.30 ± 2.02 cm^{-1} for PVA/SA, while the FWHM increased from 77.52 ± 3.77 cm^{-1} to 112.80 ± 7.44 cm^{-1} (Fig. 2c). Consistent with the trend observed for the -OH band, the blue shift and broadening of the $-COO^-$ band indicated a perturbed carboxylate environment in PVA/SA, further supporting SA-induced restructuring of local noncovalent interactions within the network. No new FTIR bands attributable to covalent bond formation were detected, consistent with a predominantly physically associated PVA/SA network mediated by noncovalent interactions.

To optimize the electrochemical impedance of the PVA/SA hydrogel for EEG bioelectronic interfacing, PEDOT:PSS was incorporated as a conductive phase. The PEDOT:PSS concentration was systematically varied, and the impedance response was quantified by electrochemical impedance spectroscopy (EIS). Across the 0-10 wt% PEDOT:PSS range, the impedance magnitude at 10 Hz (|Z| at 10 Hz) exhibited a non-monotonic dependence on composition, reaching a minimum at approximately 5 wt%, accompanied by a phase shift toward 0° (Fig. 2d). Accordingly, within the narrower 4.0-6.5

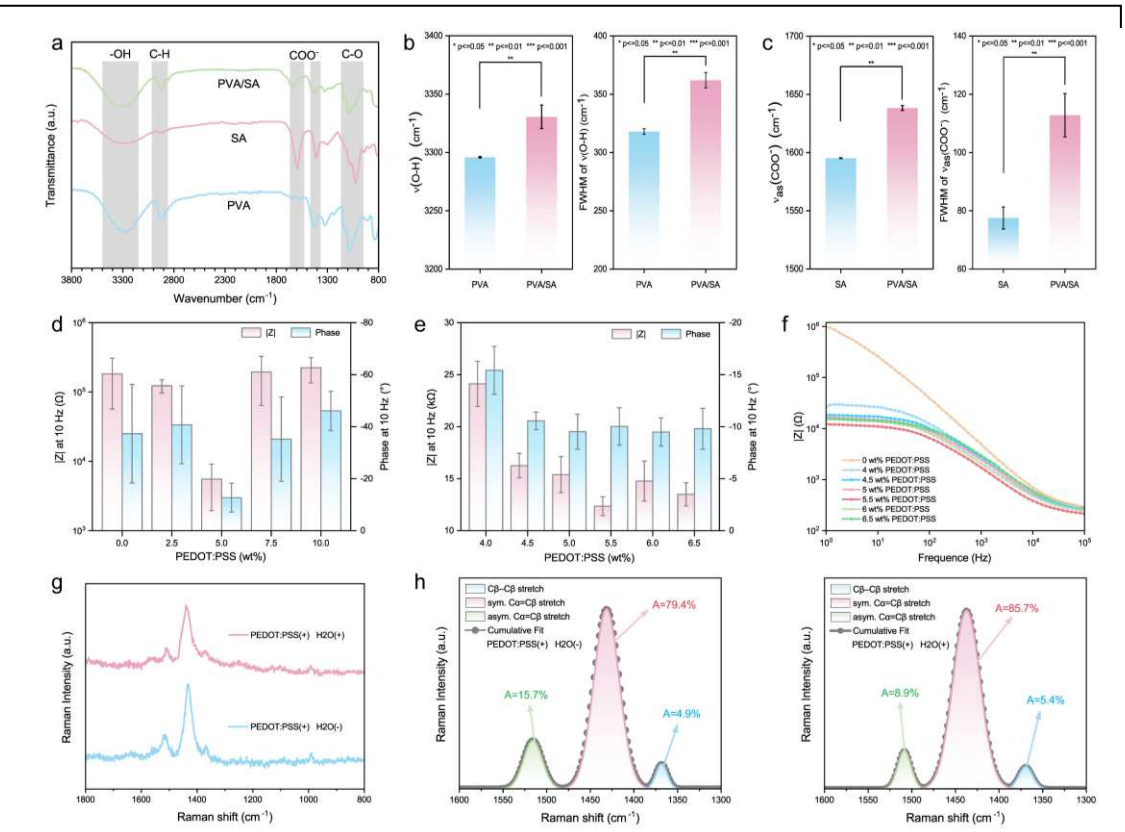


Fig. 2 Characterization of the PVA/SA/PEDOT:PSS hydrogel.

(a) FTIR spectra of PVA, SA, and PVA/SA hydrogel. (b) Peak position and FWHM of the O-H stretching band (3000-3600 cm^{-1}) for PVA and PVA/SA hydrogels. (c) Peak position and FWHM of the asymmetric $-COO^-$ stretching band (1550-1650 cm^{-1}) for SA and PVA/SA hydrogels. (d) Impedance at 10 Hz for hydrogels with PEDOT:PSS concentrations ranging from 0 to 10 wt%. (e) Impedance at 10 Hz for hydrogels with PEDOT:PSS concentrations ranging from 4.0 to 6.5 wt%. (f) Representative impedance spectroscopy of hydrogels with different PEDOT:PSS concentrations. (g) Raman spectra of the 5.5 wt% hydrogel in dry and hydrated states. (h) Deconvolution of the Raman spectra in the PEDOT fingerprint region.

wt% composition window, statistical analysis of multiple independent samples confirmed that the 5.5 wt% formulation exhibited the lowest mean |Z| at 10 Hz (Fig. 2e). Further analysis showed that the |Z| at 10 Hz of the 5.5 wt% formulation was significantly lower than that of the adjacent lower-concentration formulation, whereas the difference relative to the adjacent higher-concentration formulation was not statistically significant (Fig. S1). Consistent with this result, the impedance magnitude spectra showed that the 5.5 wt% formulation maintained the lowest impedance across the measured frequency range, with the clearest separation at low frequencies (Fig. 2f). Equivalent-circuit fitting using an R(QR) model (Fig. S2) indicated that the pronounced impedance reduction was primarily attributed to a marked decrease in the charge-transfer resistance (R_{ct}), from ~1.12×10^6 Ω in the undoped sample to ~1.37×10^4 Ω in the 5.5 wt% formulation (Fig. S3). On this basis, the 5.5 wt% formulation was selected for

all subsequent characterization and performance evaluation.

Raman spectra of the 5.5 wt% hydrogel collected over 800-1800 cm^{-1} revealed characteristic PEDOT fingerprint bands in both the dry and hydrated states (Fig. 2g). Spectral deconvolution further showed a hydration-associated redistribution of vibrational intensities, characterized by an enhanced symmetric Cα-Cβ stretching mode and a reduced asymmetric component (Fig. 2h). This spectral evolution was consistent with an increased proportion of quinoid-like segments in the PEDOT chains under hydrated conditions, suggesting hydration-associated modulation of the polymer conformation. The O-H stretching band (3000-3800 cm^{-1}) was further deconvoluted for hydrogels with and without PEDOT:PSS (Fig. S4). The closely matched component area fractions indicated that incorporation of PEDOT:PSS largely preserved the hydrogen-bonding network of the PVA/SA matrix. Combined with the impedance analysis, these results suggested that hydration-associated structural modulation of PEDOT:PSS may have contributed to the reduced interfacial charge-transfer resistance without substantially disrupting the hydrogel network.

To address interfacial mismatch caused by hair obstruction and scalp curvature, we engineered the hydrogel into a comb-shaped array of four independently compliant tines. These tines interdigitated with hair and conformed to local scalp topography, thereby improving contact consistency in hair-bearing scalp regions (Fig. 1). For stable overnight EEG acquisition, we fabricated a monolithic silicone-hydrogel composite. This was achieved by patterning comb-like grooves in a silicone scaffold and casting the hydrogel in situ, forming hydrogel tines mechanically interlocked with the silicone skeleton. The silicone scaffold reinforced the overall geometry and served as a water-vapor barrier that mitigated hydrogel dehydration, thereby stabilizing the skin-electrode interface for 8-h overnight monitoring.

2. Mechanical characterization of the hydrogel electrode

Mechanical properties were characterized under monotonic tensile loading to assess the soft, conformal mechanical compliance of the hydrogel (Fig. 3a). Uniaxial tensile tests showed that PVA hydrogels exhibited a Young's modulus of 74.2 ± 2.2 kPa and a fracture strain of 371.9 ± 23.8%, whereas PVA/SA hydrogels exhibited a markedly reduced Young's modulus of 25.8 ± 3.0 kPa (an approximately 65% decrease) while maintaining a high fracture strain of 387.8 ± 48.8% (Fig. 3b). The ultimate tensile strength decreased from 945.9 ± 306.2 kPa for PVA to 236.2 ± 45.4 kPa for PVA/SA, and toughness decreased from 1.271 ± 0.501 MJ m^{-3} to 0.391 ± 0.170 MJ m^{-3} (Fig. 3c). This pronounced softening, achieved without ionic crosslinking, was consistent with the formation of a reversible network governed by physical entanglements and dynamic hydrogen bonding.

As shown in Fig. 3d, incorporation of PEDOT:PSS endowed the hydrogel with high deformability under tensile loading. The Young's modulus was reduced to 5.9 ± 0.9 kPa,

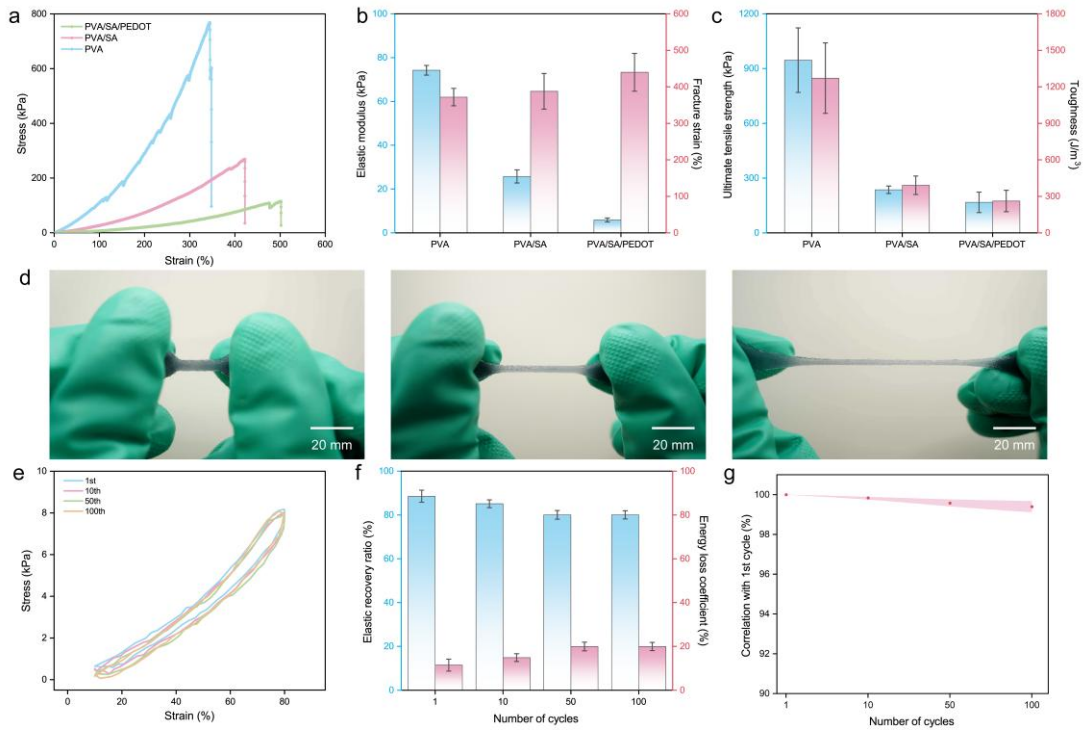


Fig. 3 Mechanical properties of the hydrogel electrodes.

(a) Representative stress-strain curves of PVA, PVA/SA, and PVA/SA/PEDOT:PSS hydrogels. (b) Young's modulus and fracture strain of PVA, PVA/SA, and PVA/SA/PEDOT:PSS hydrogels. (c) Ultimate tensile strength and toughness of PVA, PVA/SA, and PVA/SA/PEDOT:PSS hydrogels. (d) Photographs of PVA/SA/PEDOT:PSS hydrogel manually stretched to different lengths, demonstrating its high deformability. (e) Cyclic tensile loading-unloading curves of the PVA/SA/PEDOT:PSS hydrogel over 100 cycles. (f) Elastic recovery and energy loss coefficient of the PVA/SA/PEDOT:PSS hydrogel over 100 cycles. (g) Correlation coefficient between each cycle and the first cycle during cyclic tensile testing.

approximately 92% lower than that of the pure PVA hydrogels, while the fracture strain increased to 439.8 ± 51.7% (Fig. 3b). The ultimate tensile strength and toughness further decreased to 116.6 ± 61.2 kPa and 0.190 ± 0.133 MJ m^{-3}, respectively (Fig. 3c). These results indicated that incorporation of the conductive phase maintained high deformability while significantly reducing the modulus, which was favorable for conformal contact on hair-bearing scalp regions. Cyclic deformation was then characterized to assess the mechanical stability of the hydrogel under repeated deformation (Fig. 3e). Cyclic tensile tests for 100 cycles (10-80% strain) demonstrated that the PVA/SA/PEDOT:PSS hydrogel maintained a high elastic recovery of 0.834 ± 0.012 and a low energy loss coefficient of 0.166 ± 0.012 (Fig. 3f). The loading-unloading curves remained highly consistent with the first-cycle response (r = 0.997 ± 0.0009), indicating excellent cyclic stability (Fig. 3g).

The silicone exhibited a Young's modulus of 36.47 ± 1.86 kPa and a fracture strain of 231.37 ± 14.51% (Fig. S5). This modulus hierarchy, combined with the ultrasoft conductive hydrogel, mechanically buffered external loading and reduced stress transmission to the

interface during wear. Cyclic tensile tests over 100 cycles showed stable viscoelastic behavior. The elastic recovery decreased slightly from 0.863 ± 0.019 to 0.820 ± 0.010, while the energy loss coefficient increased from 0.137 ± 0.019 to 0.180 ± 0.010. The cyclic curves remained highly consistent with the first-cycle response ($r \geq 0.998$). These results indicated controlled energy dissipation and reliable shape recovery, supporting wearable conformability and structural durability during use.

3. Hydration retention of the hydrogel electrode

To evaluate the water retention capacity of the electrodes during 8-h overnight monitoring, we measured the mass change of three electrode types at 25 °C and 50% relative humidity (Fig. 4a). The commercial gel and the hydrogel without silicone scaffold were

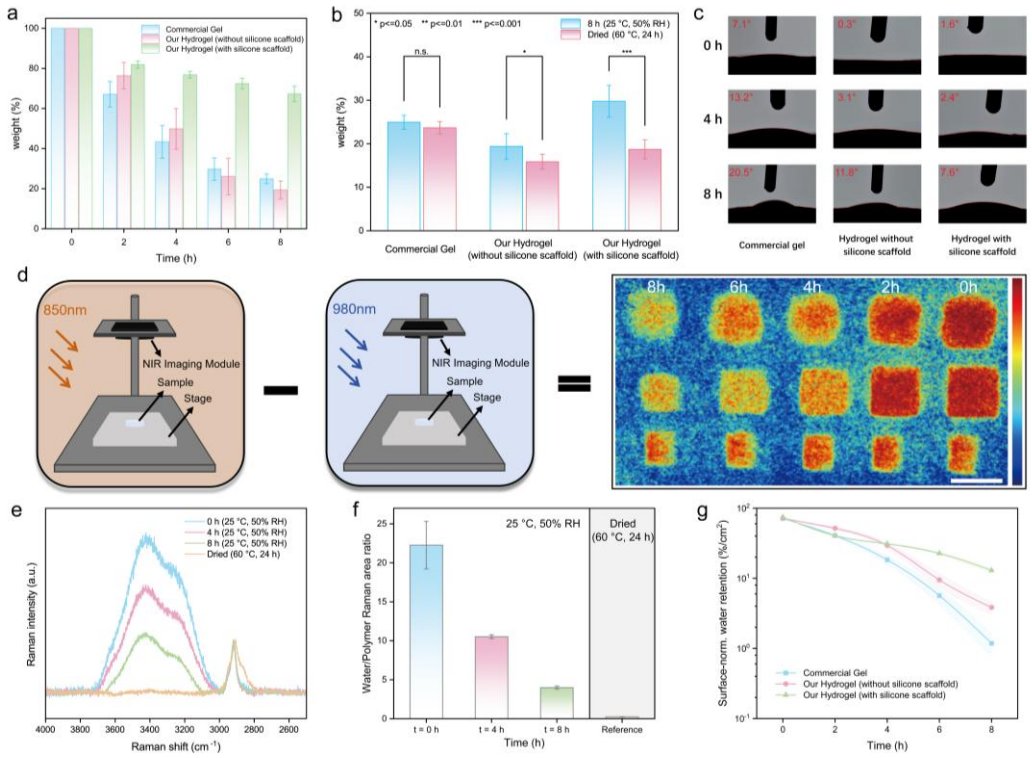


Fig. 4 Hydration retention performance of the hydrogel electrodes.

(a) Mass retention of commercial gel, hydrogel without silicone scaffold, and comb-shaped hydrogel with silicone scaffold for 8 h. (b) Mass after 8 h and completely dried mass of the three electrode types, excluding the mass of the silicone scaffold. (c) Contact angles of the three electrode types at 0 h, 4 h, and 8 h. (d) Near-infrared hydration imaging of the three electrode types, where redder colors indicate higher water content. The white scale bar represents 1 cm. The color bar indicates water content, with red representing 100% water content and blue representing 0% water content. (e) Raman spectra of the comb-shaped hydrogel with silicone scaffold at 0 h, 4 h, 8 h, and after complete drying. (f) Integrated area ratio of the O-H stretching band to the polymer backbone peak, reflecting the water content. (g) Water retention per unit area of the three electrode types over 8 h.

both square-shaped (1 cm × 1 cm × 1 mm), while the hydrogel with silicone scaffold had a comb-shaped geometry with a smaller contact area (less than 50% of the square-shaped electrodes). The commercial gel electrode lost mass rapidly, retaining only 25.0% of its initial mass after 8 h, which was not significantly different from its completely dried mass (23.7%, $p > 0.05$), indicating complete dehydration (Fig. 4b). In contrast, the hydrogel without silicone scaffold exhibited superior water retention during the first 4 h, with remaining masses of 76.4% and 49.9% at 2 and 4 h, respectively. This behavior likely arose from its higher initial water content (solid content: 15.9% vs. 23.7% for the commercial gel) and greater surface hydrophilicity (initial contact angle: 0.3° vs. 7.1° for the commercial gel) (Fig. 4c). After 4 h, the water loss rate accelerated, and the remaining mass dropped to 19.4% at 8 h, which remained significantly higher than its completely dried mass (15.9%, $p \leq 0.05$). Near-infrared hydration imaging revealed edge curling and uneven water distribution as dehydration progressed (Fig. 4d), suggesting that deswelling shrinkage and increased exposed area contributed to the accelerated water loss.

The hydrogel with silicone scaffold exhibited excellent water retention, retaining 67.3% of its initial mass at 8 h (Fig. 4a). This was further supported by Raman spectroscopy, which semi-quantitatively assessed water content using the integrated area ratio of the O-H stretching band to the polymer backbone peak, yielding values of 22.27 at 0 h, 10.52 at 8 h, and 0.236 after complete drying (Fig. 4e-f). After normalization to the active hydrogel area, the area-normalized retained mass percentage at 8 h was 12.97% cm^{-2} for the comb-shaped electrode, which was 3.4 times that of the hydrogel without silicone scaffold (3.83 % cm^{-2}) and 11.0 times that of the commercial gel (1.18 % cm^{-2}) (Fig. 4g). Its contact angle at 8 h was 7.6°, substantially lower than that of the hydrogel without silicone scaffold (11.8°) and the commercial gel (20.5°) (Fig. 4c). These results demonstrated that the silicone scaffold served as an effective physical hydration barrier, thereby mitigating hydrogel dehydration and providing a stable interfacial hydration environment for overnight EEG monitoring.

4. Electrochemical performance of the hydrogel electrode

To evaluate the electrochemical stability of the electrodes during 8-h overnight monitoring, we measured the impedance magnitude and phase angle at 10 Hz on forearm skin (Fig. 5a). At 0 h, the commercial gel exhibited an impedance of 54.7 ± 13.3 kΩ and a phase angle of -45.0 ± 4.4°. The hydrogel without silicone scaffold exhibited an impedance of 24.9 ± 6.5 kΩ and a phase angle of -13.2 ± 4.6°. The hydrogel with silicone scaffold exhibited an impedance of 23.6 ± 3.3 kΩ and a phase angle of -9.5 ± 3.1°. Both hydrogel electrodes exhibited significantly lower impedance and phase angle than the commercial gel ($p < 0.01$), indicating that the PVA/SA/PEDOT:PSS hydrogel system possessed favorable ionic-electronic mixed conductivity and supported efficient interfacial charge transfer. The reduced phase angle further suggested that the interface approached predominantly resistive

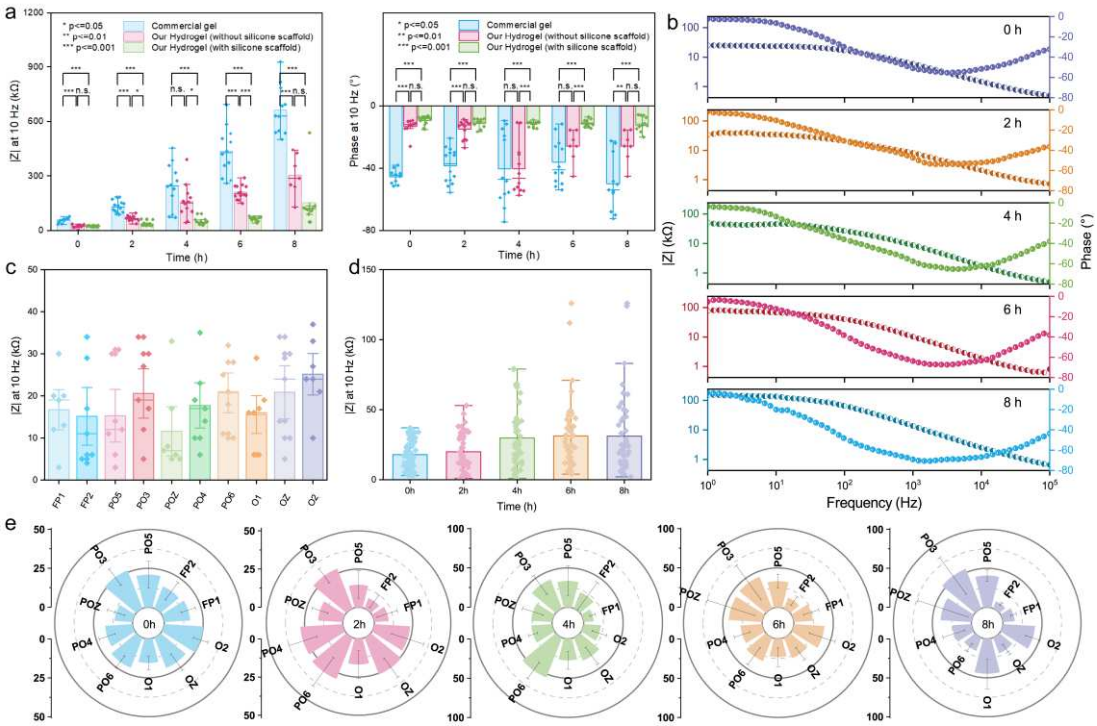


Fig. 5 Electrochemical performance of the hydrogel electrodes.

(a) Impedance at 10 Hz for commercial gel, hydrogel without silicone scaffold, and comb-shaped hydrogel with silicone scaffold at 0, 2, 4, 6, and 8 h. (b) Representative impedance spectroscopy of the comb-shaped hydrogel with silicone scaffold at 0, 2, 4, 6, and 8 h. (c) Impedance at 10 Hz across ten EEG recording sites. (d) Average impedance at 10 Hz across ten EEG sites at 0, 2, 4, 6, and 8 h. (e) Impedance at 10 Hz for each EEG site at 0, 2, 4, 6, and 8 h.

behavior. At 8 h, the impedance of the commercial gel increased to 654.5 ± 156.2 kΩ. In comparison, the impedance of the hydrogel without silicone scaffold increased to 300.4 ± 104.1 kΩ, while that of the hydrogel with silicone scaffold increased to only 108.9 ± 42.5 kΩ. The commercial gel and the hydrogel without silicone scaffold exhibited large fluctuations and significant data dispersion, whereas the phase angle of the hydrogel with silicone scaffold remained stable. These results indicated that the comb-shaped hydrogel with silicone scaffold provided a uniform and stable electrochemical interface, ensuring reliable signal acquisition during 8-h overnight monitoring. We further characterized the electrochemical impedance spectra of the hydrogel with silicone scaffold at 0, 2, 4, 6, and 8 h (Fig. 5b). Within the low-frequency range relevant to EEG signals, both the impedance magnitude and phase angle remained stable.

To further validate the on-scalp performance of the hydrogel with silicone scaffold, we measured the impedance at ten EEG recording sites (FP1, FP2, PO5, PO3, POZ, PO4, PO6, O1, OZ, O2) (Fig. 5c). Statistical analysis showed no significant differences among sites, and the average impedance across the ten sites was 20.1 ± 11.6 kΩ at 0 h (Fig. 5c). These data

suggested that the electrode provided comparable contact performance across different scalp regions, including both hairless and hair-bearing scalp regions. The average impedances at 0, 2, 4, 6, and 8 h were 20.1 ± 11.6, 19.8 ± 13.6, 29.8 ± 22.1, 31.2 ± 25.4, and 31.2 ± 28.5 kΩ, respectively (Fig. 5d). Statistical analysis showed no significant differences among time points, supporting good temporal stability during 8-h monitoring. The impedance data for each recording site at all time points are shown in Fig. 5e, further supporting spatially consistent contact performance and temporal stability on the scalp.

5. SSVEP-based EEG acquisition and system validation

We constructed an asynchronous SSVEP-based intelligent assistive care system for nighttime assistive monitoring using the comb-shaped silicone-scaffolded hydrogel electrode (Fig. 6a). The electrodes were placed at ten EEG recording sites, with FP1 and FP2 used for blink detection and the remaining eight sites used for SSVEP signal acquisition. Baseline noise levels under resting conditions are shown in Fig. 6b. The average baseline noise levels were 8.79 ± 6.27 μV in the hairless region (FP1, FP2) and 8.78 ± 1.96 μV in the hair-bearing scalp regions (PO5, PO3, POZ, PO4, PO6, O1, OZ, O2), with no significant difference between the two regions ($p > 0.05$), indicating consistent signal acquisition performance on both hairless and hair-bearing scalp regions. The SNRs of blink signals recorded from FP1 and FP2 were 26.26 ± 2.28 dB and 25.58 ± 2.80 dB, respectively, with representative waveforms shown in Fig. 6c.

The system employed a three-class SSVEP paradigm with stimulation frequencies of 9.6 Hz (emergency call), 12 Hz (toileting assistance), and 14.4 Hz (safety reset). Three consecutive blinks were used as the trigger signal, hereafter referred to as a triple blink. Upon detecting a triple blink, the system activated flicker stimulation and executed the corresponding command based on the recognized frequency. The overall workflow is illustrated in Fig. 6a and Video S1. The system achieved 100% triple-blink detection accuracy and 97.3 ± 0.4% SSVEP classification accuracy (Fig. 6d), with no significant differences among subjects ($p > 0.05$). As shown in Fig. 6e, the SNR for triple-blink (amplitude-based) was 11.81 ± 2.23 dB, while the SNRs for SSVEP (power-based) were 7.52 ± 0.27 dB (9.6 Hz), 7.25 ± 0.18 dB (12 Hz), and 7.42 ± 0.23 dB (14.4 Hz), with no significant differences among the three frequencies ($p > 0.05$). The corresponding power spectra are shown in Fig. 6f.

We further evaluated the stability of the electrode during 8-h overnight monitoring. Triple blink detection accuracy remained 100% at all time points. SSVEP recognition accuracy was 96.8 ± 3.0% (0 h), 98.4 ± 2.2% (2 h), 97.8 ± 2.4% (4 h), 97.3 ± 2.6% (6 h), and 97.8 ± 2.4% (8 h) (Fig. 6g). As shown in Fig. 6h, triple blink SNRs were 11.81 ± 2.23 dB (0 h), 11.93 ± 1.62 dB (2 h), 11.05 ± 1.82 dB (4 h), 11.81 ± 2.10 dB (6 h), and 12.30 ± 2.49 dB (8 h). SSVEP SNRs were 7.40 ± 0.23 dB (0 h), 7.51 ± 0.41 dB (2 h), 7.48 ± 0.45 dB (4 h), 7.43 ± 0.42 dB (6 h), and 7.39 ± 0.43 dB (8 h). No significant differences were observed in

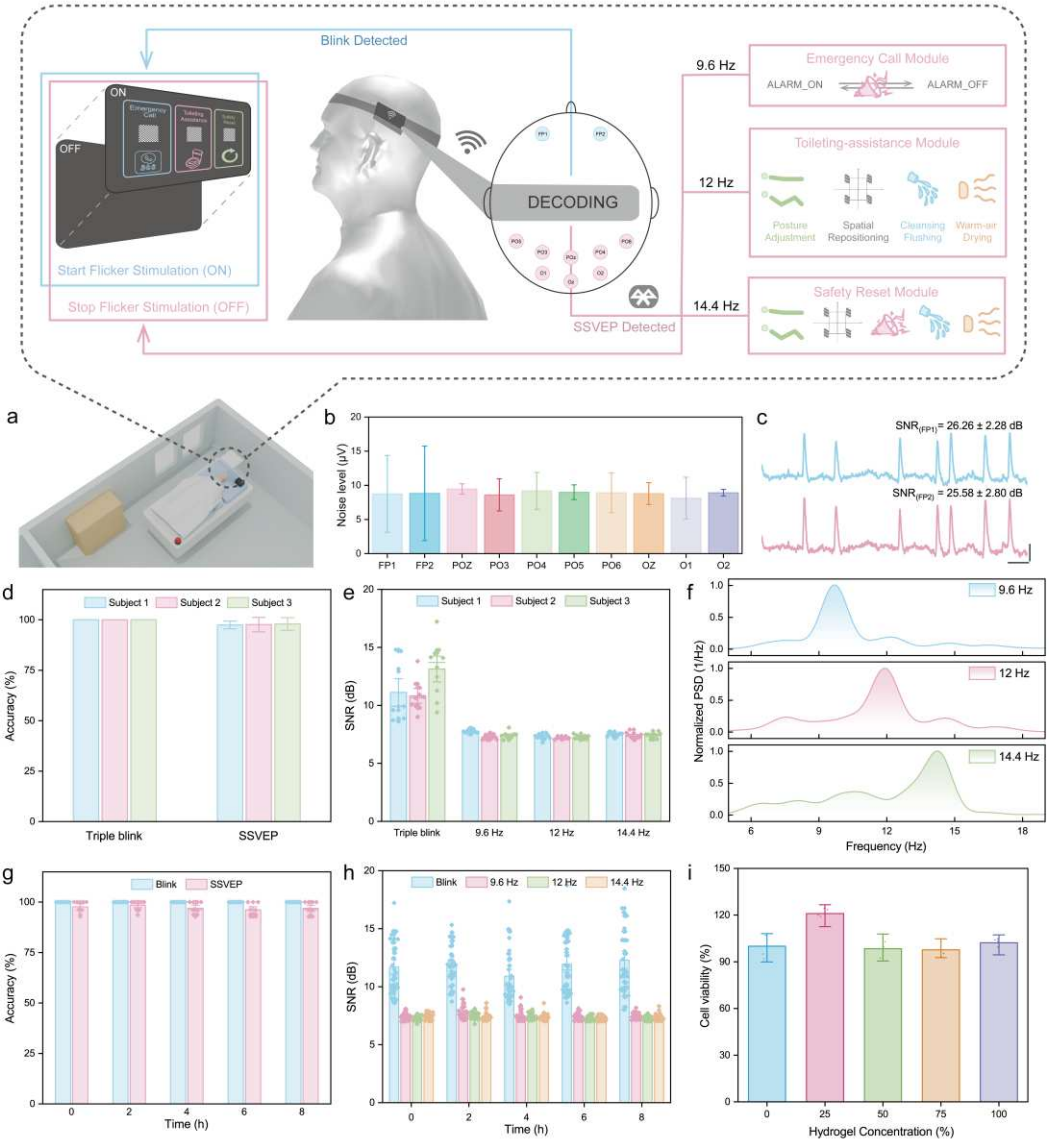


Fig. 6 SSVEP-based intelligent assistive care system validation.

(a) Schematic of the asynchronous SSVEP-based intelligent assistive care system. (b) Baseline noise levels in hairless (FP1 and FP2) and hair-bearing scalp regions. (c) Representative blink signals recorded from FP1 and FP2. The horizontal black bar represents 1 second, and the vertical black bar represents 100 μV. (d) Triple-blink detection accuracy and SSVEP classification accuracy across different subjects. (e) SNR for triple-blink detection and SSVEP classification at different frequencies across different subjects. (f) Power spectra for SSVEP signals at 9.6 Hz, 12 Hz, and 14.4 Hz. (g) SSVEP classification accuracy over 8 h. (h) Triple-blink SNR and SSVEP SNR over 8 h. (i) Cell viability of L929 fibroblasts after exposure to different concentrations of hydrogel extract.

blink or SSVEP SNRs across different time points. These results demonstrated that the electrode maintained stable performance during 8-h overnight monitoring.

Wear comfort was evaluated using a visual analog scale (VAS, 0-10, with 0 indicating no discomfort and 10 indicating extreme discomfort). All scores were below 3 (Fig. S6),

indicating minimal perceived discomfort during 8-h overnight monitoring. Cytotoxicity was assessed using the CCK-8 assay. As shown in Fig. 6i, cell viabilities for the 0%, 25%, 50%, 75%, and 100% extract groups were 100.0 ± 7.8%, 121.0 ± 5.0%, 98.4 ± 6.3%, 97.7 ± 5.4%, and 100.0 ± 4.7%, respectively, indicating no obvious cytotoxicity under the tested extract conditions.

Discussion

Hydrogel electrodes can improve prolonged scalp EEG acquisition due to their soft mechanical compliance and electrolyte confinement, which promote conformal contact and stable interfacial ionic conduction. However, hydrogel dehydration and unstable contact on hair-bearing scalp regions remain important challenges for overnight monitoring. In this work, a comb-shaped, silicone-scaffolded hydrogel electrode was developed to address these limitations. The hydrogel provided a soft conductive interface, PEDOT:PSS reduced the charge-transfer resistance, the comb-shaped structure improved contact in hair-bearing scalp regions, and the silicone scaffold suppressed dehydration.

By integrating material composition and structural design, the proposed electrode showed better hydration retention and more stable electrochemical performance. These properties were associated with stable scalp impedance and reliable EEG acquisition from both hairless and hair-bearing scalp regions over 8 h. The electrode also supported highly accurate triple-blink detection and SSVEP classification in our asynchronous SSVEP-based assistive care system during overnight use, with good subjective comfort and no obvious cytotoxicity.

These findings suggest that the proposed hydrogel electrode provides a practical strategy for stable and comfortable overnight scalp EEG acquisition. The scalp impedance showed no significant change over 8 h, further indicating good temporal stability of the electrode-skin interface during overnight monitoring. Together with the stable performance in the asynchronous SSVEP-based assistive care system, these results support its use in reliable overnight assistive BCI applications.

Materials and Methods

1. Materials

Polyvinyl alcohol (PVA, catalog #P139535, 98.0-99.0 mol% hydrolysis, viscosity 54.0-66.0 mPa·s, Aladdin, China), sodium alginate (SA, catalog #S100128, AR, Aladdin, China), poly(3,4-ethylenedioxythiophene):poly(styrenesulfonate) (PEDOT:PSS, catalog #P191136, PEDOT:PSS = 1:6, 1.5 wt% dispersion in water, Aladdin, China), potassium chloride (KCl, catalog #P301833, 99% purity, Aladdin, China), and silicone elastomer (Ecoflex 00-30, Smooth-On, USA) were used. Commercial EEG gel (Easy Gel, ZPTC, China) was used as a reference for comparison. All chemicals were used as received without further

purification. Deionized (DI) water was used throughout all experiments.

2. Preparation of PVA/SA/PEDOT:PSS hydrogel

Polyvinyl alcohol (PVA, 2.4 g), sodium alginate (SA, 0.3 g), and potassium chloride (KCl, 1.15 g) were added to deionized water (20 g) and heated in a 90 °C water bath with continuous stirring for 90 minutes to obtain a homogeneous polymer solution. Subsequently, PEDOT:PSS dispersion was added at varying concentrations (0-10 wt% relative to the total polymer mass) and stirred for an additional 30 minutes. The mixture was then degassed under vacuum to remove air bubbles. The resulting solution was cast into molds and subjected to three cycles of freezing at -20 °C for 24 h followed by thawing at 25 °C for 6 h. The as-prepared hydrogels were stored in a sealed container at 4 °C prior to use.

3. Fabrication of comb-shaped silicone-scaffolded hydrogel

The comb-shaped silicone scaffold was designed with four tines to accommodate hair-bearing scalp regions. To fabricate the scaffold, Part A and Part B of Ecoflex 00-30 were mixed at a 1:1 weight ratio, degassed under vacuum, and poured into a flat mold with an initial casting thickness of approximately 0.25 cm. The mold was placed in an oven at 60 °C for 1 h to obtain a fully crosslinked silicone sheet. A CO_2 laser cutter was then used to process the cured silicone sheet into a comb-shaped structure. By controlling the laser power and scanning path, grooves were ablated in the tines and the base region, while retaining a solid silicone layer of approximately 0.03 cm at the bottom and sidewalls of the grooves, thereby forming the hydrogel filling cavities. The laser-cut silicone scaffold was ultrasonically cleaned with ethanol to remove residual laser ablation debris, followed by ultrasonic cleaning with deionized water, and then dried for later use. Subsequently, the PVA/SA/PEDOT:PSS hydrogel precursor solution was cast into the cavities of the silicone scaffold. The assembly was then subjected to the freeze-thaw cycles to allow the hydrogel to form in situ within the cavities, resulting in an integrated silicone-hydrogel composite electrode in which the silicone scaffold supports the overall geometry and suppresses water loss, while the contact-facing hydrogel remains exposed for scalp contact. The final electrode dimensions were approximately 0.6 cm × 0.8 cm, with each tine measuring approximately 0.1 cm × 0.5 cm.

4. Spectroscopic and morphological characterization

FTIR spectra were recorded using a Nicolet 6700 spectrometer (Thermo Fisher Scientific, USA) in attenuated total reflectance (ATR) mode. Hydrogel samples were freeze-dried prior to measurement. Spectra were collected over the range of 400-4000 cm^{-1} with a resolution of 2 cm^{-1} and 10 scans per sample. Gaussian fitting of the hydroxyl stretching region (3000-3600 cm^{-1}) and asymmetric carboxylate stretching region (1550-1650 cm^{-1}) was performed to analyze peak position and full width at half maximum (FWHM). Raman spectra were acquired using an inVia confocal Raman microscope (Renishaw, UK) with a 532 nm

excitation laser. Spectra were collected over the range of 800-1800 cm^{-1} for PEDOT fingerprint bands and 3000-3800 cm^{-1} for the O-H stretching band. Hydrated samples were measured immediately after removal from storage, and dried samples were obtained after drying in an oven at 60 °C for 24 h. Spectral deconvolution was performed using Gaussian-Lorentzian functions. The morphology of the hydrogel electrode was characterized using a scanning electron microscope (VEGA3 SBH, TESCAN, Czech Republic). Samples were freeze-dried prior to measurement and sputter-coated with a thin layer of gold to enhance conductivity. Images were acquired at an accelerating voltage of 5 kV.

5. Mechanical characterization

Uniaxial tensile tests were performed using a universal testing machine (ZQ-990B, ZHIQU, China) equipped with a 50 N load cell. Hydrogel samples were cut into dumbbell-shaped specimens and tested at a crosshead speed of 20 mm/min until failure. Young's modulus was calculated as the slope of the linear region (0-10% strain). Fracture strain was determined at the point of sample rupture, and toughness was calculated as the area under the stress-strain curve. Cyclic tensile tests were conducted at a strain amplitude of 10-80% for 100 cycles, with a loading/unloading rate of 30 mm/min. Elastic recovery was calculated as the ratio of recovered strain to applied strain, and energy loss coefficient was determined as the ratio of hysteresis loop area to loading work.

6. Hydration retention measurement

Water retention of the hydrogels was evaluated by monitoring mass changes over time under ambient conditions (25 °C, 50% relative humidity). Three electrode types were tested: commercial gel (1 cm × 1 cm × 1 mm), hydrogel without silicone scaffold (same dimensions), and comb-shaped hydrogel with silicone scaffold (total area < 50% of the square electrodes). The initial mass (m_0) was recorded, and samples were placed on an open bench. At predetermined time intervals (0, 2, 4, 6, 8 h), samples were weighed (m_t), and the remaining mass percentage was calculated. To account for differences in active hydrogel area among electrode designs, an area-normalized retained mass percentage was further defined as the retained mass percentage divided by the active hydrogel area. The completely dried mass was obtained after drying at 60 °C for 24 h. Contact angle measurements were performed by depositing a 1 μL DI water droplet on the hydrogel surface. Hydration distribution was visualized using near-infrared hydration imaging.

7. Electrochemical characterization

Electrochemical impedance spectroscopy (EIS) was performed using an electrochemical workstation (CHI660E, CH Instruments, USA) with a three-electrode configuration, where the hydrogel electrode served as the working electrode, and two disposable Ag/AgCl ECG electrodes (X-1, Liya, China) were used as the reference and counter electrodes. The

impedance magnitude and phase angle were measured over a frequency range of 1 Hz to 100 kHz with an AC amplitude of 10 mV. For on-skin measurements, electrodes were placed either on the volar forearm or at ten EEG recording sites (FP1, FP2, PO5, PO3, POZ, PO4, PO6, O1, OZ, O2) according to the international 10-20 system. Impedance at 10 Hz was extracted from the spectra for comparison. Equivalent circuit fitting was performed with an R(QR) model. Charge transfer resistance (R_{ct}) was obtained from the fitting results.

8. EEG acquisition and validation of the SSVEP-based system

All experiments were approved by the Research Ethics Committee of Tsinghua University (No. THU-01-2025-1017). Informed consent was obtained from all participants. Ten EEG recording sites (FP1, FP2, PO5, PO3, POZ, PO4, PO6, O1, OZ, O2) were prepared according to the international 10-20 system. The comb-shaped silicone-scaffolded hydrogel electrodes were applied directly to the scalp without skin preparation. The electrodes were fixed on the scalp with gauze to ensure stable contact. Reference and ground electrodes were placed on the bilateral mastoids. EEG signals were recorded using a biosignal amplifier (NeuSen W, Borui Kang, China) with a sampling rate of 1200 Hz. Signals were bandpass filtered (0.5-50 Hz) and a notch filter (50 Hz) was applied to remove power line interference. A three-class SSVEP paradigm was implemented with stimulation frequencies of 9.6 Hz (emergency call), 12 Hz (toileting assistance), and 14.4 Hz (safety reset). Visual stimuli were presented on a 24-inch LCD monitor (refresh rate 144 Hz). Each stimulus was a square checkerboard pattern flickering at the designated frequency. Subjects were positioned 50 cm from the monitor and instructed to focus on the target stimulus. Three consecutive blinks were used as the trigger signal to initiate the SSVEP paradigm. Blink signals were detected from the FP1 and FP2 channels.

The asynchronous SSVEP-based intelligent assistive care system operated as follows: (1) The system continuously monitored EEG signals from FP1 and FP2 for triple-blink detection. (2) Upon detecting a triple blink, the system activated the flickering stimuli. (3) The subject focused on the desired stimulus corresponding to the intended command. (4) The system acquired SSVEP signals from the eight occipital and parietal channels (PO5, PO3, POZ, PO4, PO6, O1, OZ, O2) and performed frequency recognition. (5) The recognized command was then mapped to a predefined assistive function. For the 9.6 Hz emergency call function, an odd-numbered detection triggered the alarm, while an even-numbered detection turned it off. For the 12 Hz toileting assistance function, odd-numbered detections initiated the first-stage assistive sequence, including moving to the toilet, adjusting posture, and completing preparation, whereas even-numbered detections initiated the second-stage sequence, including toilet flushing, bidet washing, and drying, followed by posture restoration and returning to the room. Upon detection of the 14.4 Hz command, the system shut down, all hardware was reset to the initial state, and the detection counter was reset to zero.

9. Comfort evaluation

Wear comfort was assessed using a visual analog scale (VAS, 0-10, with 0 indicating no discomfort and 10 indicating extreme discomfort). Subjects rated their comfort level immediately after electrode application and at 0, 2, 4, 6, and 8 h during overnight monitoring.

10. Cytotoxicity assessment

Cytotoxicity of the hydrogel electrode was evaluated using the Cell Counting Kit-8 (CCK-8) assay. Hydrogel samples were extracted in cell culture medium (DMEM with 10% fetal bovine serum) at 37 °C for 24 h to obtain 100% extract. Serial dilutions (0%, 25%, 50%, 75%, and 100% extract) were prepared. L929 mouse fibroblasts were seeded in 96-well plates at a density of 1×10^4 cells per well and incubated for 24 h. The culture medium was then replaced with the extract solutions, and cells were incubated for an additional 24 h. CCK-8 reagent (10 μL per well) was added, and after 2 h of incubation, the absorbance was measured at 450 nm using a microplate reader. Cell viability was normalized to the control group (0% extract), which was set to 100%.

11. Statistical analysis

All data are presented as mean ± standard deviation (SD), unless otherwise stated. Statistical comparisons were performed using analysis of variance (ANOVA) followed by Tukey's post hoc test for multiple comparisons. Two-group comparisons were performed using Student's t-test. A p-value < 0.05 was considered statistically significant.

Acknowledgments

This work was supported by the Scientific Research Startup Foundation of Xiangtan University (22QDZ52), the Key Project of Xiangtan Municipal Science and Technology Bureau (ZX-ZD20240001).

Author contributions

C. W., W. P., and J. C. conceived the project. W. L., C. W., Y. Z., H. J., K. W., and X. W. designed and performed the experiments. W. L., C. W., Y. Z., and H. J. developed the intelligent assistive hardware system. C. W., X. G., X. L., Y. L., and G. M. analyzed the data. C. W., Y. W., and J. C. prepared the figures. C. W. and W. P. drafted the manuscript. All authors approved the final version of the manuscript.

Competing interests

The authors declare that they have no competing interests.

Supplementary information

Supplementary Fig. S1-S6 and Video S1 (illustrating the intelligent assistive care system

workflow) are available in the Supplementary Information.

References

[1] Ren L., Zhou Y., Liu K., et al. The Effect of Healthy Lifestyles and Social Determinants on Independent Life Expectancy and Sex Differences in China: Evidence from a 13-Year Cohort Study[J]. The Lancet Public Health, 2025, 10(12): e1016–e1024

[2] Feigin V. L., Abate M. D., Abate Y. H., et al. Global, Regional, and National Burden of Stroke and Its Risk Factors, 1990–2021: A Systematic Analysis for the Global Burden of Disease Study 2021[J]. The Lancet Neurology, 2024, 23(10): 973–1003

[3] Feigin V. L., Brainin M., Norrving B., et al. World Stroke Organization: Global Stroke Fact Sheet 2025[J]. International Journal of Stroke, 2025, 20(2): 132–144

[4] Suh J. W., Bell V., Buckman J. E. J., et al. A Record-Linkage Study of Post-Stroke Primary Care Psychological Therapy Effectiveness in England[J]. Nature Mental Health, 2025, 3(6): 626–635

[5] Lin Z., Qian Y., Gill T. M., et al. Absence of Care among Community-Dwelling Older Adults with Dementia and Functional Limitations[J]. Nature Aging, 2025, 5(4): 548–557

[6] Villalobos Dintrans P., Fabiani deLeva B. Challenges in Reducing Long-Term Care Needs: Insights from China[J]. The Lancet Healthy Longevity, 2025, 6(4): 100705

[7] Kim H., Won K., Ahn M., et al. A 40-Class SSVEP Speller Dataset: Beta Range Stimulation for Low-Fatigue BCI Applications[J]. Scientific Data, 2025, 12(1): 1751

[8] Chen S., Chen M., Wang X., et al. Brain–Computer Interfaces in 2023–2024[J]. Brain-X, 2025, 3(1): e70024

[9] Ding Y., Udompanyawit C., Zhang Y., et al. EEG-Based Brain-Computer Interface Enables Real-Time Robotic Hand Control at Individual Finger Level[J]. Nature Communications, 2025, 16(1): 5401

[10] Caiado F., Ukolov A. The History, Current State and Future Possibilities of the Non-Invasive Brain Computer Interfaces[J]. Medicine in Novel Technology and Devices, 2025, 25: 100353

[11] Cheng Y., Yan L., Shoukat M. U., et al. An Improved SSVEP-Based Brain-Computer Interface with Low-Contrast Visual Stimulation and Its Application in UAV Control[J]. Journal of Neurophysiology, 2024, 132(3): 809–821

[12] Gao X., Wang Y., Chen X., et al. Brain–Computer Interface—A Brain-in-the-Loop Communication System[J]. Proceedings of the IEEE, 2025, 113(5): 478–511

[13] Gao S., Chen J., Xia Y., et al. Wearable Technologies for Assisted Mobility in the Real World[J]. Nature Communications, 2025, 16(1): 10988

[14] Bayat M., Safaie J., Beidokhti S. M., et al. A Comprehensive Review of EEG Electrode Technologies: Advancements, Applications, and Future Directions[J]. Sensors and Actuators A: Physical, 2026, 399: 117396

[15] Lin S., Jiang J., Huang K., et al. Advanced Electrode Technologies for Noninvasive Brain–Computer Interfaces[J]. ACS Nano, 2023, 17(24): 24487–24513

[16] Wang Z., Shi N., Zhang Y., et al. Conformal In-Ear Bioelectronics for Visual and Auditory Brain-Computer Interfaces[J]. Nature Communications, 2023, 14(1): 4213

[17] Pei W., Wu X., Zhang X., et al. A Pre-Gelled EEG Electrode and Its Application in SSVEP-Based BCI[J]. IEEE Transactions on Neural Systems and Rehabilitation Engineering, 2022, 30: 843–850

[18] Wang W., Xu G., Huang K., et al. Cholinium-Based Eutectogel Electrode for High-Quality Dynamic EEG/ECG Monitoring Exceeding 48 Hours[J]. npj Flexible Electronics, 2025, 9(1): 121
[19] Zhang R., Wen S., Zhao Y., et al. Water-Removable Paste Electrode for Electrophysiological Monitoring on Hairy Skin[J]. ACS Applied Electronic Materials, 2025, 7(2): 925–932
[20] Xue H., Wang D., Jin M., et al. Hydrogel Electrodes with Conductive and Substrate-Adhesive Layers for Noninvasive Long-Term EEG Acquisition[J]. Microsystems & Nanoengineering, 2023, 9(1): 79
[21] Xu D., Meng X., Liu S., et al. Dehydration Regulates Structural Reorganization of Dynamic Hydrogels[J]. Nature Communications, 2024, 15(1): 6886
[22] Zhang A., Shyam A. B., Cunningham A. M., et al. Adhesive Wearable Sensors for Electroencephalography from Hairy Scalp[J]. Advanced Healthcare Materials, 2023, 12(22): 2300142
[23] Zhang M., Qian B., Gao J., et al. Recent Advances in Portable Dry Electrode EEG: Architecture and Applications in Brain-Computer Interfaces[J]. Sensors, 2025, 25(16): 5215
[24] Xiong F., Fan M., Feng Y., et al. Advancements in Dry and Semi-Dry EEG Electrodes: Design, Interface Characteristics, and Performance Evaluation[J]. AIP Advances, 2025, 15(4): 040703
[25] Zhang L., Kumar K. S., He H., et al. Fully Organic Compliant Dry Electrodes Self-Adhesive to Skin for Long-Term Motion-Robust Epidermal Biopotential Monitoring[J]. Nature Communications, 2020, 11(1): 4683
[26] Li G. L., Wu J. T., Xia Y. H., et al. Review of Semi-Dry Electrodes for EEG Recording[J]. Journal of Neural Engineering, 2020, 17(5): 051004
[27] Liu J., Lin S., Li W., et al. Ten-Hour Stable Noninvasive Brain-Computer Interface Realized by Semidry Hydrogel-Based Electrodes[J]. Research, 2022, 2022: 2022/9830457
[28] Wang D., Xue H., Xia L., et al. A Tough Semi-Dry Hydrogel Electrode with Anti-Bacterial Properties for Long-Term Repeatable Non-Invasive EEG Acquisition[J]. Microsystems & Nanoengineering, 2025, 11(1): 105
[29] Zhu Y., Bayin C., Li H., et al. A Flexible, Stable, Semi-Dry Electrode with Low Impedance for Electroencephalography Recording[J]. RSC Advances, 2024, 14(46): 34415–34427
[30] Xiao M., Zhang X., Luo Y., et al. Engineering Hydrogel-Based Conformal Epidermal Electrodes for Human-Machine Interaction[J]. Soft Science, 2025, 5(3)
[31] Zhang Z., Yang J., Wang H., et al. A 10-Micrometer-Thick Nanomesh-Reinforced Gas-Permeable Hydrogel Skin Sensor for Long-Term Electrophysiological Monitoring[J]. Science Advances, 2024, 10(2): eadj5389
[32] Wang Y., Wang Z., Zhang Y., et al. A 2.7-Mm-Thick Robust, Permeable, and Antifreezing Hydrogel Electrode for Long-Term Ambulatory Health Monitoring[J]. Science Advances, 2025, 11(38): eadt2286
[33] Liu Y., Shen S., Duan Z., et al. Hydrogels for Long-Term Moisture Retention under Ambient Conditions: Inhibiting the Evaporation of Free Water from Macroscopic to Molecular Scales[J]. Advanced Functional Materials, 2025, 35(47): 2504356

[34] Cai D., Yu Y. Internal and External Strategies for Preventing Hydrogel Dehydration[J]. Advanced Materials Technologies, 2026, 11(5): e01756
[35] Zhu Y., Chen B., Liu Y., et al. Recent Advances in Conductive Hydrogels for Electronic Skin and Healthcare Monitoring[J]. Biosensors, 2025, 15(7): 463
[36] Bai M., Chen Y., Zhu L., et al. Bioinspired Adaptive Lipid-Integrated Bilayer Coating for Enhancing Dynamic Water Retention in Hydrogel-Based Flexible Sensors[J]. Nature Communications, 2024, 15(1): 10569
[37] Li T., Qi H., Zhao C., et al. Robust Skin-Integrated Conductive Biogel for High-Fidelity Detection under Mechanical Stress[J]. Nature Communications, 2025, 16(1): 88
[38] Liang X., Yu B., Yokota T., et al. Conforming Strategies for Bioelectronics on Arbitrary Surfaces[J]. npj Biosensing, 2025, 2(1): 41
[39] Wang C., Wang H., Wang B., et al. On-Skin Paintable Biogel for Long-Term High-Fidelity Electroencephalogram Recording[J]. Science Advances, 2022, 8(20): eabo1396
[40] Reis Carneiro M., Tavakoli M., Majidi C. Soft Skin-Interfacing Electrodes for Wearable Bioelectronics[J]. Matter, 2025, 8(10): 102409
[41] Wang Y., Wang Z., Yi J., et al. Injectable Eutectogel for High-Quality Scalp Electroencephalogram Monitoring[J]. npj Flexible Electronics, 2025, 9(1): 125
[42] Kim K., Jeong J. Y., Shin J. H., et al. Materials and Structures of Skin-Interfaced Electrodes for Reducing Motion Artifacts in Neural Recording[J]. Small Methods, 2026, 10(3): e01708
[43] Ahmed S., Momin M., Ren J., et al. Stick-and-Play Bioadhesive Hairlike Electrodes for Chronic EEG Recording on Human[J]. npj Biomedical Innovations, 2025, 2(1): 9

Supplementary Files

This is a list of supplementary files associated with this preprint. Click to download.

- ACombShapedSiliconeScaffoldedHydrogelElectrodeforStableOvernightEEGAcquisitioninAssistiveBCIApplicationsSupplementaryInformation.pdf
- WorkflowofanAsynchronousSSVEPBasedIntelligentAssistiveCareSystem.mp4